Characterizing the Three-Dimensional Structure of Block Copolymers *via* Sequential Infiltration Synthesis and Scanning Transmission Electron Tomography

Tamar Segal-Peretz,[†,‡] Jonathan Winterstein,[§] Manolis Doxastakis,[†,‡] Abelardo Ramírez-Hernández,[†,‡] Mahua Biswas,[∥] Jiaxing Ren,[†] Hyo Seon Suh,[†,‡] Seth B. Darling,[†,⊥] J. Alexander Liddle,[§] Jeffrey W. Elam,[∥] Juan J. de Pablo,[†,‡] Nestor J. Zaluzec,[⊥] and Paul F. Nealey[*,†,‡]

[†]Institute for Molecular Engineering, University of Chicago, 5747 South Ellis Avenue, Chicago, Illinois 60637, United States, [‡]Materials Science Division, [∥]Energy Systems Division, and [⊥]Center for Nanoscale Materials, Argonne National Laboratory, 9700 S. Cass Avenue, Argonne, Illinois 60439, United States, and [§]Center for Nanoscale Science and Technology, National Institute of Standards and Technology, 100 Bureau Drive, Gaithersburg, Maryland 20899, United States

ABSTRACT Understanding and controlling the three-dimensional structure of block copolymer (BCP) thin films is critical for utilizing these materials for sub-20 nm nanopatterning in semiconductor devices, as well as in membranes and solar cell applications. Combining an atomic layer deposition (ALD)-based technique for enhancing the contrast of BCPs in transmission electron microscopy (TEM) together with scanning TEM (STEM) tomography reveals and characterizes the three-dimensional structures of poly(styrene-*block*-methyl methacrylate) (PS-*b*-PMMA) thin films with great clarity. Sequential infiltration synthesis (SIS), a block-selective technique for growing inorganic materials in BCPs films in an ALD tool and an emerging technique for enhancing the etch contrast of BCPs, was harnessed to significantly enhance the high-angle scattering from the polar domains of BCP films in the TEM. The power of combining SIS and STEM tomography for three-dimensional (3D) characterization of BCP films was demonstrated with the following cases: self-assembled cylindrical, lamellar, and spherical PS-*b*-PMMA thin films. In all cases, STEM tomography has revealed 3D structures that were hidden underneath the surface, including (1) the 3D structure of defects in cylindrical and lamellar phases, (2) the nonperpendicular 3D surface of grain boundaries in the cylindrical phase, and (3) the 3D arrangement of spheres in body-centered-cubic (BCC) and hexagonal-closed-pack (HCP) morphologies in the spherical phase. The 3D data of the spherical morphologies was compared to coarse-grained simulations and assisted in validating the simulations' parameters. STEM tomography of SIS-treated BCP films enables the characterization of the exact structure used for pattern transfer and can lead to a better understating of the physics that is utilized in BCP lithography.

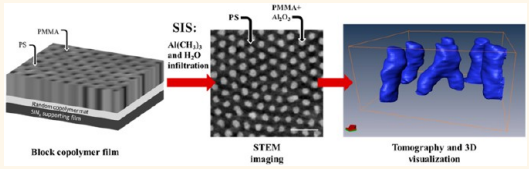

KEYWORDS: block copolymers · self-assembly · TEM · STEM · tomography · SIS

Block copolymer (BCP) lithography combines sub-20 nm features with low-cost polymer processing methods and therefore has been extensively investigated for the next generation of nanopatterning. Indeed, in the past decade, tremendous progress has been made in directing the assembly of BCPs to form the desired structure using chemical or topographical boundary conditions and transferring the BCP pattern to the underlying substrates.[1−3] Nonetheless, one of the main challenges that still remain in the field is how to characterize and fully understand the three-dimensional structure of the BCPs. Currently, the vast majority of the morphological characterization involves top-down, or plan-view scanning electron microscopy (SEM) imaging. Since plan-view SEM provides principally surface information, one must use an additional characterization method to distinguish between films with identical surface morphology but different internal structure[4,5] in order to decipher their actual three-dimensional structure. Several characterization methods have been demonstrated for revealing the three-dimensional (3D) structure of BCP thin films in real space. Among them are cross-sectional SEM imaging[5,6] and repeated plasma etching

* Address correspondence to nealey@uchicago.edu.

Received for review February 12, 2015 and accepted April 28, 2015.

Published online April 28, 2015
10.1021/acsnano.5b01013

of the film to expose the inner structure, followed by surface imaging[6−9] or surface force microscopy (SFM) imaging.[10] X-ray scattering has also been used to characterize the 3D structure of BCP thin films, but lacks the ability to study individual defects.[11] When trying to determine the 3D structure of poly(styrene-*block*-methyl methacrylate) (PS-*b*-PMMA), one of the most investigated block copolymers and a good candidate for BCP lithography in both the semiconductor and bit-patterned media industries, high-resolution cross-sectional SEM imaging requires careful milling and polishing, and results in a relatively small imageable area,[4,5] while etching the film has been known to cause artifacts in the structure. Transmission and/or scanning transmission electron microscopy (TEM/STEM) tomography, on the other hand, can directly resolve three-dimensional structures with high resolution and provide information that is not accessible by cross-sectional SEM.[12]

Electron tomography has been demonstrated as an excellent tool for understanding BCP structure in order−order transitions[13−16] and BCP assembly under confinement,[17,18] as a complementary tool for reflectivity and scattering methods,[19,20] and to investigate the structure of directed self-assembled BCPs.[21] The contrast mechanism in TEM imaging of BCP specimens is mainly mass−thickness contrast; thus, most BCPs generally suffer from poor contrast in the TEM since they do not contain any high atomic number scatterers. As a consequence of this, BCP specimens are usually chemically treated, or stained, using conventional staining agents such as OsO_4 and I_2 to increase their scattering contrast during imaging studies. There is a concern, however, that the staining process can swell the nanophase domains[22] or lead to morphological artifacts, resulting in characterization of a structure different from the block copolymer structure that would later be used for pattern transfer.

Recently, sequential infiltration synthesis (SIS), an emerging materials growth technique derived from atomic layer deposition (ALD),[23−25] has been shown to enhance etch contrast between the blocks of BCPs and transform the block copolymer template into an efficient hard mask for pattern transfer.[26−29] The SIS process is based on the selective growth of various inorganic species within the polar blocks of BCPs (such as PMMA or poly(vinylpyrrolidone) (PVP)).[25] The most common SIS-based pattern transfer process consists of three steps. In the first step, Al_2O_3[30] is grown from trimethylaluminum (TMA) and water gas-phase precursors in an ALD chamber using conditions as described previously.[24] During the SIS process, the precursors diffuse through the BCP film. TMA interacts preferentially with PMMA as a result of the interaction of the electrophilic aluminum atom in TMA with the nucleophilic oxygen atom of the carbonyl group of PMMA. This leads to selective growth of Al_2O_3 in the polar BCP blocks. With repeated SIS cycles, more TMA infiltrates into the polymer film, resulting in higher Al_2O_3 content.[24,31] In the second step, the film is exposed to short oxygen plasma to remove the organic material, followed by the third step, where the pattern is transferred to the underlying substrate using reactive ion etching.[27]

In this study, we show that Al_2O_3 SIS significantly enhances the contrast in STEM imaging and allows detailed investigation with great fidelity of self-assembled BCP structures using annular dark-field (ADF) imaging and subsequent tomographic reconstruction. By tuning the SIS process conditions, high contrast imaging in ADF-STEM can be achieved while following the original BCP morphology; thus, the first step in the SIS-based pattern transfer process could be investigated. To study the effect of SIS on ADF-STEM imaging, lamellae-forming, cylinder-forming, and sphere-forming PS-*b*-PMMA films were studied prior to and after the SIS process. This high contrast and the apparently sharp PS−PMMA interface revealed by the Al_2O_3 grown in the SIS process provide a path to high-resolution characterization of PS-*b*-PMMA three-dimensional structures, including phase morphology, grain boundaries, and the 3D structure of defects.

By employing quantitative tools such as Delaunay triangulation and unit-cell orientation maps on self-assembled PS-*b*-PMMA cylinders' tomography data, we were able to delineate the depth profile of various defects and grain boundaries. This analysis revealed that 5-fold and 7-fold dislocation defects that occur at high and low grain boundaries do not necessarily persist perpendicularly through the film, but rather change location or split into two cylinders through the film's thickness. Tomography data can also complement molecular simulation, as demonstrated for sphere-forming PS-*b*-PMMA films. Characterization of the 3D structure of sphere-forming PS-*b*-PMMA films with body-centered-cubic (BCC) or hexagonal-close-packed (HCP) morphology was obtained using ADF-STEM tomography of SIS-treated films. The 3D structures were consistent with coarse-grained models of the same samples, revealing the local organization of spheres in both morphologies.

RESULTS AND DISCUSSION

Sample Preparation. Samples were prepared for TEM imaging in the following manner (Figure 1): a silicon wafer with a ≈100 nm water-soluble poly(acrylic acid) (PAA) layer on it was used as a substrate. The substrate's chemistry was modified by spin coating ≈8 nm of a random copolymer mat layer on the PAA layer. The mat's chemistries, *i.e.*, the styrene fraction in the mats, were chosen in order to have a homogeneous surface that would induce perpendicular orientation in lamellae and cylindrical BCP assembly and highly ordered spherical BCP assembly. Then, lamellae-forming,

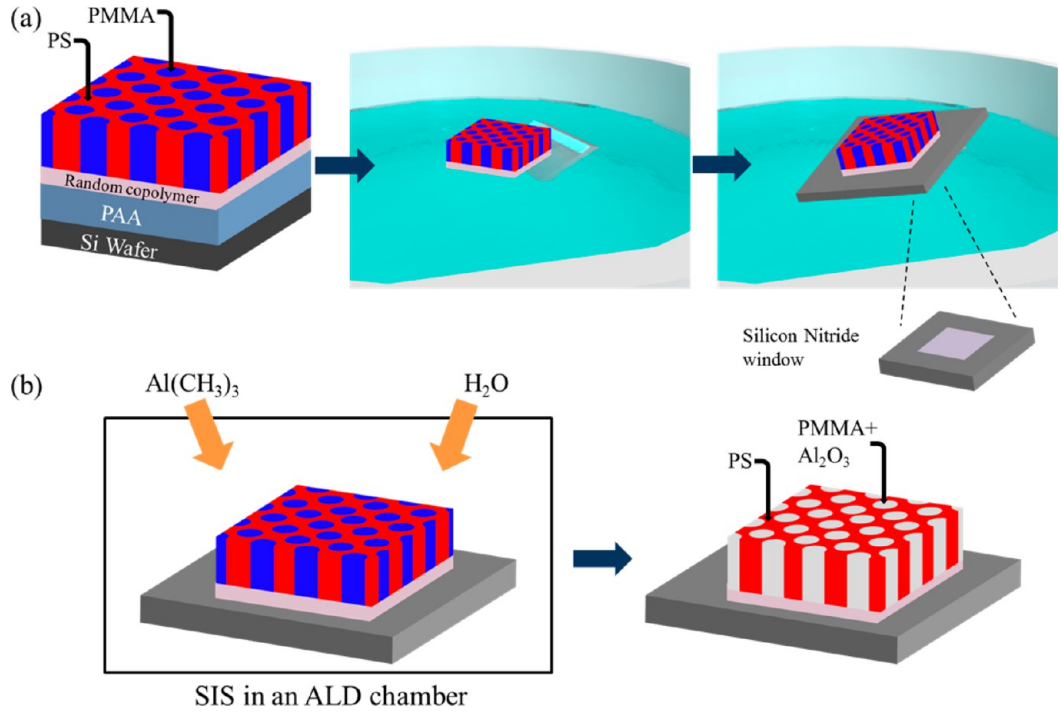

Figure 1. Schematic illustration of the sample preparation process. (a) PS-*b*-PMMA BCP thin film (50−80 nm in thickness) self-assembled on a random copolymer mat layer on top of a water-soluble poly(acrylic acid) (PAA) layer. The BCP film and the random copolymer film were floated off in water and scooped up using a silicon nitride window designed for TEM tomography imaging. (b) Silicon nitride window with the polymer layers on top treated with three cycles of SIS in an ALD chamber, resulting in incorporation of Al_2O_3 within the PMMA domains.

cylinder-forming, or sphere-forming PS-*b*-PMMA films (50−80 nm in thickness and domain spacing (L_0) of 40, 38, and 48 nm, respectively) were self-assembled on the random copolymer mats (see Experimental Methods for more details). To enable TEM imaging, the BCP layer and the random copolymer layer were floated in deionized water and were transferred to a silicon nitride window (50 nm thick). To enhance the contrast in ADF-STEM imaging and enable tomographic study of the BCPs, Al_2O_3 was grown mainly in the PMMA domains *via* three cycles of SIS in an ALD chamber. Previous studies of SIS have shown that by tuning the SIS parameters, a relatively uniform concentration of Al_2O_3 throughout the film's depth can be achieved even with film thicknesses of 200−300 nm.[26,31] Thus, the contrast in ADF-STEM imaging is expected to remain constant through the film's depth in the films investigated in this study.

Tomographic Methodology in SIS-Treated BCP Films. To date, most block copolymer tomography has been conducted using (parallel-beam) TEM imaging.[32,33] STEM imaging, however, offers a number of potential advantages over TEM imaging for block copolymer tomography. In STEM tomography, a focused electron probe is raster-scanned over the specimen, while the scattered or unscattered transmitted electrons forming the images are detected by an annular dark-field detector or bright-field detector, respectively. The images are recorded as in the TEM mode, while the specimen is tilted over an angular range of up to ±70°. Since the image contrast in ADF-STEM is roughly proportional to Z^2, where Z is the atomic number,[34] it is expected that the addition of elements like aluminum (13) and oxygen (8) *via* the SIS process will significantly enhance the imaging contrast in the ADF-STEM mode. Importantly, the STEM probe focus is dynamically adjusted under microprocessor control to correct for effects of specimen tilt, which facilitates imaging over large field of views, while it is not possible to implement an equivalent correction in the TEM mode. STEM tomography also provides independent control over the probe size and scanning rate, enabling a straightforward approach to minimizing radiation damage. In addition, the elastic scattering events that give rise to the contrast in ADF-STEM imaging make this method less sensitive to chromatic aberration of the objective lens and to the increased inelastic scattering that occurs in thick specimens. These effects would otherwise contribute to the diffuse image background and a corresponding loss of contrast. ADF-STEM therefore provides a means of imaging moderately thick films (>50 nm) with high resolution and high signal-to-noise ratio, which is desired in block copolymer characterization.[35,36] For these reasons, STEM tomography has been widely adopted by the life science community.[37,38] While it has also been demonstrated for polymer materials,[35,36] it has not yet been applied to BCP tomography.

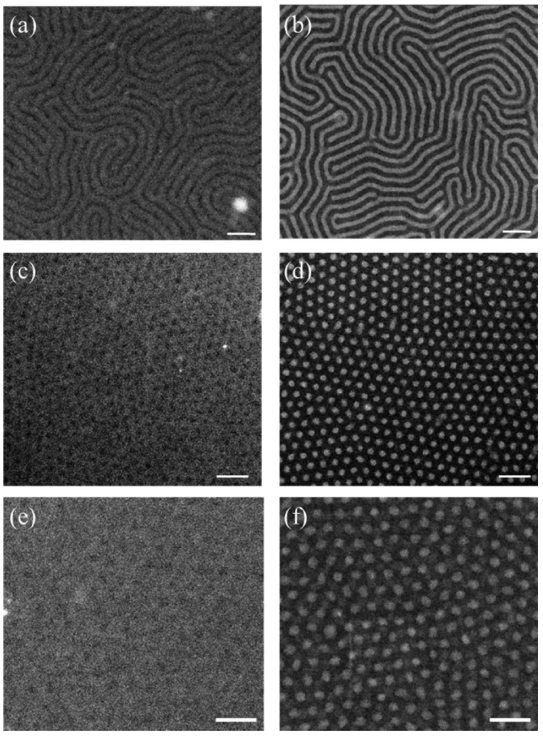

Figure 2. Effect of SIS on PS-*b*-PMMA STEM imaging. STEM images of lamellae-forming PS-*b*-PMMA (37k−37k, a, b), cylinder-forming PS-*b*-PMMA (46k−21k, c, d), and sphere-forming PS-*b*-PMMA (72k−12k, e, f) as prepared (a, c, e), and after three cycles of Al_2O_3 SIS (b, d, f). Scale bars are 100 nm.

In order to demonstrate the influence of the SIS process on PS-*b*-PMMA STEM imaging, lamellae-forming, cylinder-forming, and sphere-forming PS-*b*-PMMA films were imaged as prepared and after three cycles of Al_2O_3 SIS (Figure 2). Images of the as-prepared film and the SIS-treated film of the same BCP were acquired under identical conditions. A significant increase in contrast can be seen in SIS-treated films (Figure 2b, d, and f) compared with the as-prepared films (Figure 2a, c, and e). The enhancement in contrast is due to the increased high-angle scattering that occurs from the alumina in the PMMA domains, which are collected by the ADF-STEM detector. The addition of alumina also results in contrast reversal; in the as-prepared film, the bright domains are PS and the PMMA domains appear darker, whereas in the SIS-treated films the bright regions are from the strongly scattering PMMA domains with the alumina infiltrated into them, while the PS domains are darker. In addition, since the STEM images of the as-prepared films are constructed mainly from electrons that interact with the PS domains, it becomes more difficult to resolve the PMMA domains in films with lower PMMA volume fractions. Thus, morphologies such as body-centered-cubic spheres (volume fraction of PMMA = 0.13) are barely resolved (Figure 2e). The SIS-treated films, on the other hand, show enhanced contrast and sharp interfaces between the PS and the PMMA domains, enabling cylinders and spheres to be easily resolved.

The depth of field in STEM can be controlled by controlling the convergence angle.[34,36] Here, for film thicknesses of 50 to 80 nm, a convergence angle of 14 mrad, which can be easily achieved in noncorrected STEM, creates a large enough depth of field to resolve two distinct layers of spheres. For thicker samples, a smaller convergence angle and correspondingly larger depth of field can be used to form focused images of the entire thickness of the film. As mentioned earlier, the SIS-treated films exhibit a sharp interface between the BCP domains. We hypothesize that this sharp interface originates from the incorporation of the highly scattering alumina in the entire PMMA domain, including in the domain's (mixed) interface where PS and PMMA chains are intermixed, and that is usually observed as a PS domain. Contrast enhancement as well as sharp interface between the blocks can also be seen in TEM imaging of the same films (Supporting Information, Figure S1). However, because phase-contrast TEM imaging contrast is ultimately less sensitive to atomic number than in ADF-STEM, the enhancement in contrast is less pronounced.

In order to study the origin of the contrast enhancement and verify that Al_2O_3 is embedded in the PMMA domains, we have investigated the elemental distribution of the BCP films after three cycles of Al_2O_3 SIS using X-ray energy dispersive spectroscopy (XEDS)-STEM elemental mapping. As can be seen in Figure 3a−c, both aluminum (Figure 3b) and oxygen (Figure 3c) are present mainly in one of the domains, which is correlated to the bright domains in the ADF-STEM image of the same region (Figure 3a), indicating that the Al_2O_3 is incorporated in the PMMA domains. The aluminum K signal is attributed to the Al_2O_3, while the oxygen signal originates both from Al_2O_3 and from PMMA's acrylate groups. The intensity line profile of the ADF detector signal together with aluminum and oxygen K shell emission line profiles (Supporting Information, Figure S2) also shows good agreement between the bright PMMA domains and the location of aluminum and oxygen elements. The carbon elemental map (Figure 3d) shows a higher carbon signal in the PS domains than in the PMMA domains due to the higher carbon density in the PS domains (2:1 mol carbon/cm^3 in PS:PMMA). To verify the uniformity across the 128 × 128 pixel elemental maps, a Si elemental map was also simultaneously collected and is presented (Figure 3e), showing uniform Si intensity that originates from the silicon nitride supporting film. The elemental distribution study therefore corroborates the presence of alumina in the PMMA domains and sheds light on the origin of contrast enhancement in SIS-treated PS-*b*-PMMA films.

Evidence that the domain periodicity of the block copolymer (L_0) was not altered by the SIS conditions used here and that swelling of the PMMA domain was minimal was derived from both the PMMA cylinders'

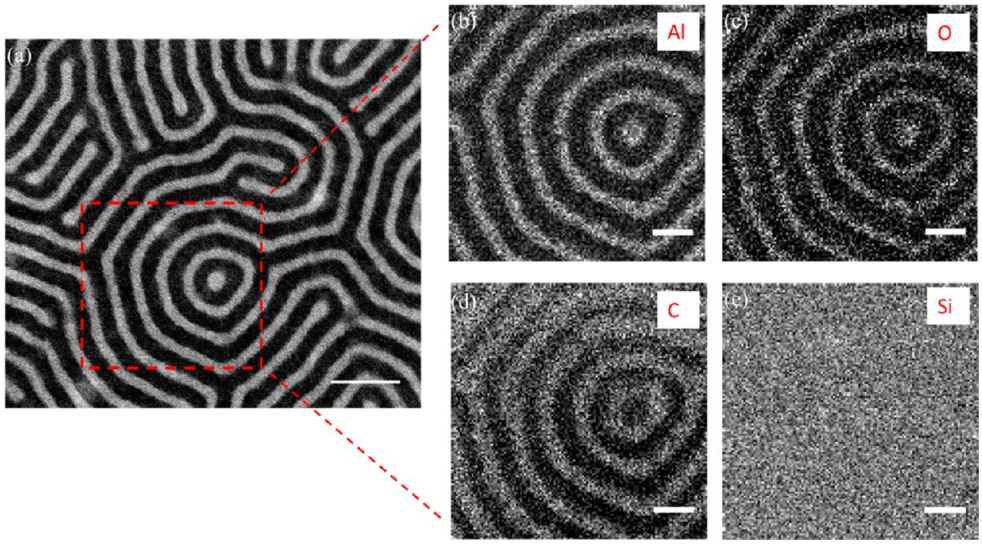

Figure 3. XEDX-STEM mapping of lamellae-forming PS-*b*-PMMA. (a) ADF-STEM image of lamellae-forming PS-*b*-PMMA after three cycles of Al_2O_3 SIS; (b)−(e) corresponding elemental mapping of aluminum, oxygen, carbon, and silicon K X-ray lines, respectively. Scale bars are 50 nm.

center-to-center distance and the PMMA cylinders' size, *i.e.*, the cross-sectional area perpendicular to the cylinder axis in the cylinder-forming SIS-treated film. The center-to-center measurements of cylinder-forming PS-*b*-PMMA (black histogram, Figure 4a) exhibit a normal distribution (red line, Figure 4a) corresponding to an L_0 of 38.6 ± 2.4 nm (all measurements are shown as average ± one standard deviation). The variation in cylinder spacing is primarily due to the actual variability in the film, which includes defects and grain boundaries. The average L_0 is in excellent agreement with previously published neutron scattering measurements of a similar polymer.[39] This agreement is particularly encouraging given the ability of scattering measurements to provide precise statistics over large areas. The Al_2O_3 content in the polar domains, and hence the swelling of the domains, can be controlled by the number of cycles and additional parameters in the SIS process. A study by Biswas *et al.* on the growth mechanism of Al_2O_3 in the SIS process has shown that only 5% of the carbonyl groups in a PMMA film react with the TMA in the first SIS cycle;[31] thus, it is anticipated that Al_2O_3 can be grown within the PMMA domain with minimal swelling. To accurately measure the cylinder diameter, the cylinders' cross-sectional areas were measured using particle size analysis (see Experimental Methods for details), and the diameter was calculated from the cross-sectional area under the assumption that the cross-section is a perfect circle. The cylinder diameter (black histogram, Figure 4b) also exhibits a normal distribution (red line, Figure 4b) with an average diameter of 19.9 ± 2.2 nm, which is in good agreement with theoretical calculations based on the volume fraction of PMMA in a unit cell (22.0 nm). The above measurements corroborate that, with three cycles of SIS, sufficient Al_2O_3 was grown to enable high-contrast ADF-STEM imaging while domain swelling was kept minimal.

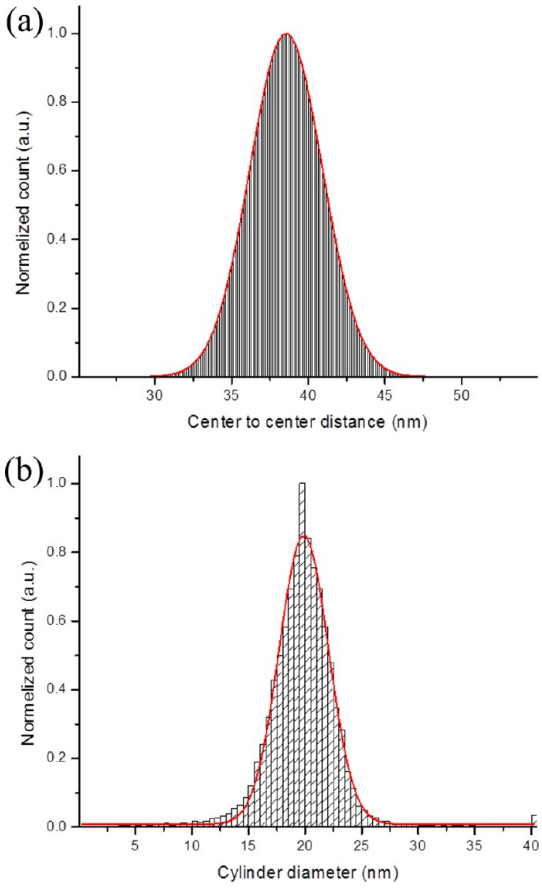

Figure 4. Quantitative analysis of ADF-STEM imaging of a cylinder-forming PS-*b*-PMMA film treated with three cycles of Al_2O_3 SIS. Measured distribution (black histogram) and fitted Gaussian curve (red line) of (a) cylinder spacing by center-to-center measurements and (b) cylinder diameter extracted from face area measurements.

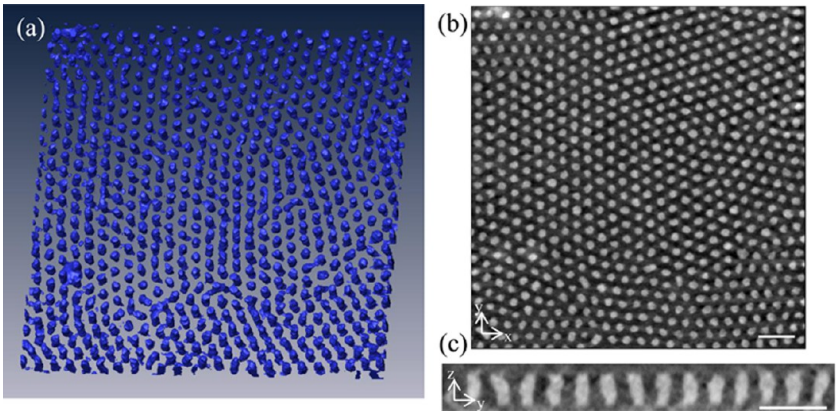

Figure 5. ADF-STEM tomography of cylinder-forming PS-*b*-PMMA treated with three cycles of Al_2O_3 SIS: (a) visualization of the 3D reconstructed volume. For clarity PMMA domains are colored in blue, while PS domains are transparent. The dimensions of the reconstructed volume are 910, 930, and 60 nm (*x*, *y*, *z*). (b) A 1.1 nm thick *xy* slice of the reconstructed volume taken from the middle of the film (*z* = 25.3 nm). (c) A 1.1 nm thick *yz* digitally sliced cross section of the reconstructed volume taken from the central grain. Scale bars are 100 nm.

Good contrast between domains is a necessary condition for tomography, but it is not sufficient. Another condition that must be met is the stability of the sample under the electron beam. In SIS-treated BCP films, both the polymer and the Al_2O_3 pose a challenge in terms of stability.[40,41] Nonetheless, by carefully tuning the microscope conditions, high contrast and stability could be achieved with an electron dose range of 150 to 600 e/Å^2 per image, while the film lacks any apparent structural change. For example, after continuous scanning in the ADF-STEM of a lamellae-forming PS-*b*-PMMA film treated with three cycles of Al_2O_3 SIS for 80 min using a 200 e/Å^2 dose and 60 s scan time per image (Supporting Information Figure S3), no structural damage or carbon contamination could be detected. The total dose in this series of images (16 000 e/Å^2) is 60% higher than the total dose in the typical tomography experiments we have performed in this work. BCP films treated with Al_2O_3 SIS, therefore, exhibit the sufficient stability for acquiring a tilt series for tomographic analysis.

Tomographic Results of SIS-Treated BCP Films. The enhanced contrast and high stability of SIS-treated specimens under ADF-STEM conditions described above enable a three-dimensional characterization of PS-*b*-PMMA BCP films using STEM tomography. SIS-treated cylinder-forming, lamellae-forming, and sphere-forming PS-*b*-PMMA BCP films with thicknesses of 50 to 80 nm were characterized using ADF-STEM tomography, and the results are presented in Figure 5, Figure 8, and Figure 9, respectively.

A. Cylinder-Forming BCP. Visualization of the 3D reconstructed volume of cylinder-forming PS-*b*-PMMA (Figure 5a) highlights the rich three-dimensional data that can be obtained by tomography, including the structure of perpendicular PMMA cylinders, defects in the self-assembled film, and grain boundaries. For clarity, the PMMA domains are colored blue, while the PS domains are rendered transparent. The dimensions of the reconstructed volume are 910, 930, and 60 nm (*x*, *y*, *z*); a movie presenting different view perspectives of the visualized volume is available in the Supporting Information (Movie 1). Notably, performing tomography of a thin film as opposed to traditional microtomed sections enabled us to image large fields of view encompassing both the nanostructure and the micrometer-sized grains. To better understand the structure of PMMA cylinders in the film, the reconstructed volume was digitally sliced into *xy* and *yz* slices (*xy* is the plane parallel to the substrate surface, and *z* is the direction of the film surface's normal). A 1.1 nm thick *xy* slice (Figure 5b), taken from the middle of the film ($z = 25.3 \pm 1.1$ nm above the substrate interface; details about *z* height calculations are presented in the next paragraph and in the Experimental Methods), shows the typical hexagonal morphology of self-assembled cylinder-forming PS-*b*-PMMA with the cylinder axis perpendicular to the substrate. The digitally sliced *yz* cross sections (Figure 5c) show the structure of perpendicular cylinders normal to the substrate with an average cylinder diameter of 20.0 ± 1.1 nm and cylinder spacing of 38.5 ± 1.3 nm, which matches the measurements performed on the 2D projection of the volume (Figure 2d).

We have further studied the cylindrical structure as a function of depth using the *xy* slice series. The series, consisting of 46 slices, each ~1.1 nm thick, starts at the film's surface ($z = 49.5$ nm) and at the film's bottom interface with the random copolymer mat ($z = 0$ nm; see Experimental Methods for *z* height calculation details). The cylinders' center-to-center distances (L_0) and the cylinders' diameters were measured in each slice in the majority of the volume ($5.5 \text{ nm} \leq z \leq 42.9$ nm). The average values of both measurements as a function of *z* height are presented in the Supporting Information (Figure S4a and b, respectively).

The average center-to-center distance shows uniform values across the entire depth (38.7 ± 0.1 nm), while the average cylinder diameter is uniform in the majority of the depth (19.8 ± 1.5 nm) with only a small decrease in the cylinders' diameters close to the bottom interface. As previously discussed, the average values are in quantitative agreement with data from scattering techniques that probe large sample areas, a result that supports the precision of SIS-treated ADF-STEM tomography. This is particularly encouraging given the ability of STEM tomography to complement material characterization with unique structural information at local length scales. We will further discuss in the following sections the three-dimensional information obtained from sparse defects that have minimal contributions to the average structure.

As expected from a self-assembled film, defects can be seen in the visualized volume both at grain boundaries and as isolated defects. Defects in a perpendicular-cylinder hexagonal lattice have been described by Hammond *et al.*[42] and others[43−45] as dislocation defects and can be easily identified by their coordination number. Typically, 5-fold and 7-fold coordination defects occur in pairs, and the defect's domains adjust their size and spacing to mitigate the stress associated with the grain boundary. Up until now, these defects have been studied by surface analysis using SEM or SFM imaging,[42−45] and questions such as "is a defect seen at the film's surface also present in the interior of the film?" and "what is the three-dimensional structure of an individual defect?" have been investigated in nondirect methods using pattern transfer.[43,45] With TEM tomography, however, one can study how defects arrange in 3D as well as their spatial distribution as a function of depth. To investigate the three-dimensional behavior of defects, we have analyzed the *xy* slice series using Delaunay triangulation of the centers of PMMA domains. The analysis is presented in Figure 6a, b, and c, as well as in Movie 2 (Supporting Information). Delaunay triangulation analysis identifies well-organized regions where cylinders have 6-fold coordination (not colored), *versus* defects with 5-fold (or less) coordination (blue circles) and 7-fold (or more) coordination (red circles). Application of this analysis on the *xy* slice series probes the organization as a function of depth and allows complete characterization of these defects. Figure 6a presents an example of this analysis performed at $z = 9.9$ nm, showing multiple 5-fold and 7-fold defects within the film's depth. The fascinating 3D behavior of these defects is revealed by examining the *xy* slice series. For example, in the Delaunay triangulation analysis performed near the top of the film in the area marked with a yellow rectangle in Figure 6a and presented in Figure 6b, two trio defects are observed, with a 5-fold/8-fold/5-fold structure ($z = 38.5 \pm 1.1$ nm and $z = 37.4 \pm 1.1$ nm, marked with white arrows). The 8-fold cylinders at the center of the trio are actually short cylinders parallel to the film's surface, which then split into two cylinders perpendicular to the film's surface. This splitting results in 6-fold-coordinated cylinders, as can be seen from the perfect organization of cylinders at those areas in Delaunay triangulation analysis performed at $z = 36.3$ nm and $z = 35.2$ nm. Another example can be seen in Figure 6c (red rectangle in Figure 6a). Here, the 7-fold cylinder that is seen at $z = 20.9 \pm 1.1$ nm and is marked with a white arrow stretches and widens with depth ($z = 14.3 \pm 1.1$ nm and $z = 11.0 \pm 1.1$ nm), until at $z = 9.9$ nm it splits into two perpendicular cylinders, resulting in one 6-fold cylinder and one 5-fold cylinder and displacing the dislocation pair to a new *xy* location.

To better understand the correlation between the defects' *z* profile and the grain boundaries, it is convenient to look at the order parameter for bond orientations (ψ):

$$\psi(\vec{r}) = e^{6i\theta(\vec{r})} \quad (1)$$

where $\theta(\vec{r})$ is the orientation relative to some fixed reference axis of the bond between two neighboring atoms or in this case of the intercylinder bond obtained by Delaunay triangulation.[46] We have calculated the modulus $\pi/3$ of $\theta(\vec{r})$ of the *xy* slice series and present them in color maps of unit-cell orientation, where the colors of the unit-cell orientation indicate a range from 0 to $\pi/3$ relative to an arbitrary vector (Figure 6d and e; Movie 3, Supporting Information). It is known that dislocation lines arise to delimit two grains with a high-angle grain boundary, *i.e.*, where φ, the orientation mismatch angle between two adjacent grains, is between 15° and 30°, while isolated dislocations arise when $\varphi < 15°$.[43] Indeed, a comparison between the unit-cell orientation maps and Delaunay triangulation analysis (for example, Figure 6a and d) shows that both isolated defects and dislocation lines exist through the entire thickness of the film. The depth profile of the grain boundaries can be precisely followed by examining the unit-cell orientation color maps of the *xy* slice series. Figure 6e shows the grain boundary (marked with a dashed white line) as a function of depth in the area marked with a white rectangle in Figure 6d. This grain boundary arises between the central grain in the field of view (red) and the bottom grain in the field of view (blue), which have a 30° angle between them. Interestingly, even in this thin film (50 nm; 1.3 L_0), the grain boundary is not a surface perpendicular to the substrate but rather has a variable *xy* position through the film, forming a curved surface in *z*. In addition, the unit-cell orientation maps reveal interesting behavior of the defects at the grain boundaries. Two examples are observed in Figure 6e (highlighted by white arrows in Figure 6e and by dashed white circles in Movie 3). In example number one, a cylinder close to the grain boundary but within the blue grain is seen at $z = 26.4$ nm.

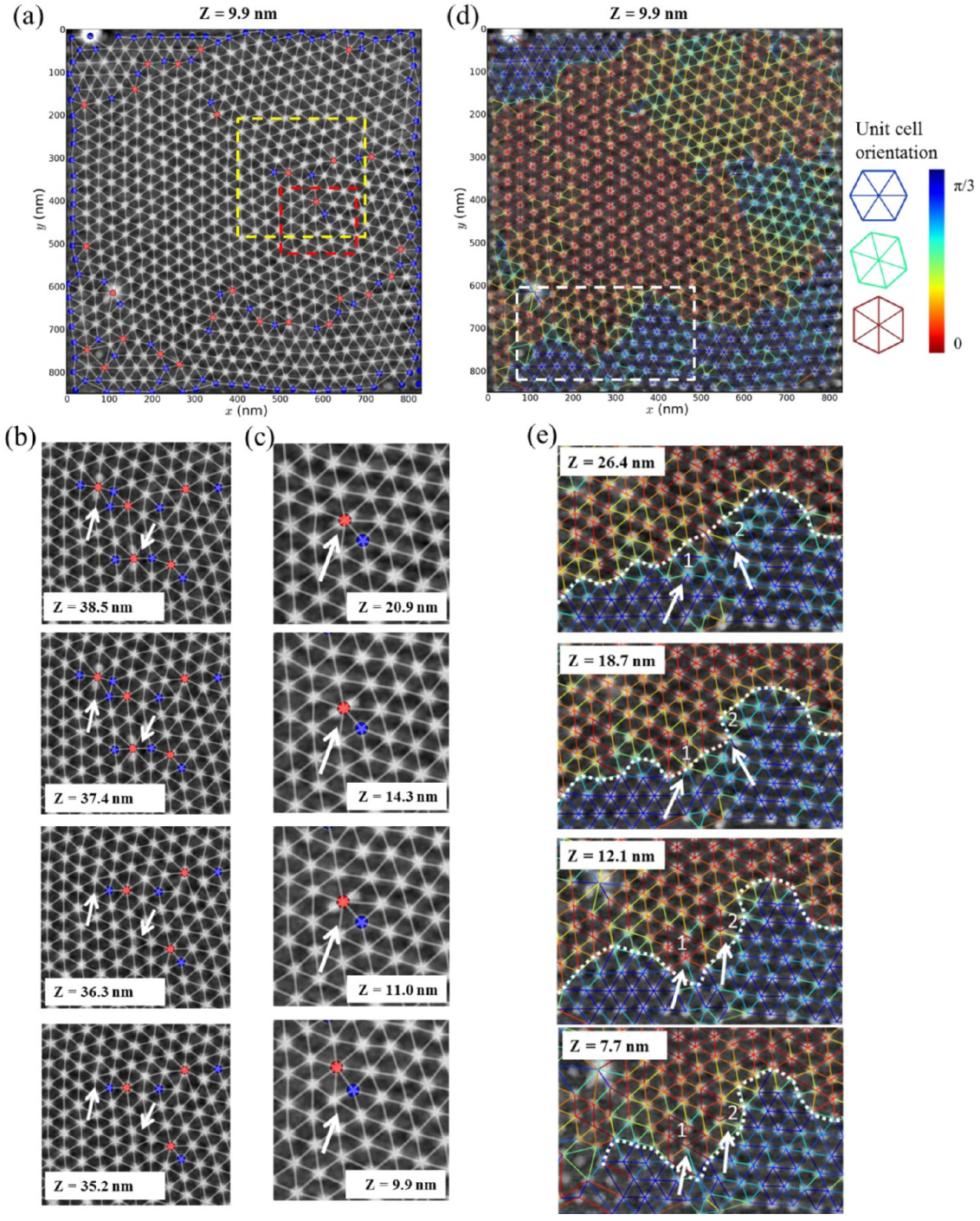

Figure 6. Quantitative analysis of 1.1 nm thick *xy* slice series obtained from ADF tomography of cylinder-forming PS-*b*-PMMA treated with three cycles of Al_2O_3 SIS. (a) Delaunay triangulation analysis of the *xy* slice at *z* = 9.9 nm above the substrate interface. The analysis shows 6-fold cylinders (not colored) *vs* 5-fold (blue) and 7-fold (red) cylinders indicating dislocation defects. (b, c) Delaunay triangulation analysis of *xy* slices at various *z* heights at areas marked by yellow and red rectangles in (a), respectively. (d) Unit-cell orientation color map of *xy* slice at *z* = 9.9 nm above the substrate interface, where the colors of the orientation indicate a range from 0 to $\pi/3$. (e) Unit-cell orientation color map of *xy* slices at various *z* heights at area marked by white rectangle in (d).

This cylinder crosses the grain boundary and moves to the red grain with depth ($z = 12.1 \pm 1.1$ nm and $z = 7.7 \pm 1.1$ nm), forming a 30° tilting angle in the *zy* plane (Figure S5, Supporting Information). In example number two, another cylinder close to the blue–red grain boundary is seen at $z = 26.4$ nm. This cylinder splits into two cylinders at $z = 12.1$ nm exactly at the grain boundary, resulting in one cylinder in each grain. We hypothesize that the local stress created due to the discrepancy between the grain orientations together with the assembly kinetics determines the three-dimensional structure of cylinders at grain boundaries.

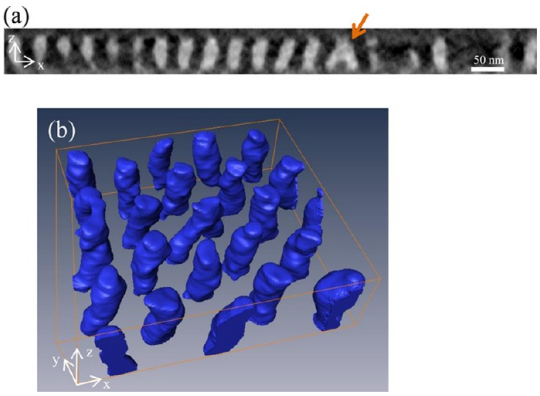

Figure 7. Three-dimensional structure of a splitting defect in the SIS-treated cylinder-forming PS-*b*-PMMA film. (a) A 1.1 nm thick *xz* slice taken at the splitting plane. (b) Visualization of the reconstructed volume of the area of the same defect.

The quantitative analysis using Delaunay triangulation and unit-cell orientation maps enabled us to track defects through the *xy* slice series and investigate their spatial distribution in 3D.

Through TEM tomography we can take our investigation of defects one step further and resolve their 3D structure. Understanding the defect's 3D structure is important for pattern transfer applications, where defects in the BCP layer will affect the structure in the underlying layer after pattern transfer. The cylinder described earlier in Figure 6e is seen through the *xy* slice series to split into two cylinders. Indeed, the digitally sliced *xz* cross section taken at the splitting plane (Figure 7a) confirms that the 3D structure of the defect is similar to an "inverted Y", where a single cylinder at the top of the film splits into two cylinders toward the bottom of the film. Moreover, a visualization of the area of the defect (Figure 7b) together with the *xz* slice (Figure 7a) shows that the cylinders around the defect tend to bend or tilt to accommodate the change in spacing that occurs due to the splitting of the central cylinder. A closer look at all the defects in the field of view reveals that eight of the defects exhibit this splitting behavior. Interestingly, we observed only a splitting behavior, while the reverse behavior where two cylinders at the top of the film merge into one cylinder toward the bottom was not observed in the field of view. This splitting behavior and the unit-cell orientation map (Figure 6d and e; Movie 3) suggest that the central grain in the field of view is larger at the bottom of the film than at top of the film. This might indicate that different kinetics or nucleation and grain coarsening occurs at the top and at the bottom of the film, although a larger number of grains must be characterized in order to better understand this phenomenon.

B. Lamellae-Forming BCP. We have also investigated lamellae-forming PS-*b*-PMMA through Al_2O_3 SIS and ADF-STEM tomography and studied their three-dimensional structures. Visualization of a 1506 nm × 1470 nm × 80 nm (*x*, *y*, *z*) reconstructed volume is presented in Figure 8a and Movie 4 (Supporting Information). For clarity, PMMA domains are colored blue, while PS domains are rendered transparent. The image shows the complex 3D structure of lamellae "fingerprint" patterns. As expected, splitting and merging of lamellae that occur underneath the film's surface, usually hidden from view when using surface characterization techniques, are revealed in the tomography data. For example, Figure 8b–d present ~1.5 nm thick *xy* slices from the top, middle, and bottom of the film, respectively, from the area marked with an orange square in Figure 8a. The slices show three individual PMMA lamellae close to the film's surface (z = 66.0 nm), merging at the middle of the film (z = 37.5 nm), and then splitting into two lamellae toward the bottom of the film (z = 19.5 nm). This example together with those examples seen in the cylinder-forming PS-*b*-PMMA film demonstrates the ability of ADF tomography of SIS-treated BCP films to decipher the 3D structure of defects and individual domains.

C. Sphere-Forming BCP. TEM tomography can be used not only to characterize a specific area or defect but also to shed light on the 3D morphology of phases. The spherical phase in BCPs is inherently a 3D structure, but has been explored experimentally mainly by surface analysis[47] and scattering methods.[48,49] However, none of the above methods have been able to reveal the 3D morphology in real space and probe in detail the local arrangement of the BCP domains. Indeed, Stein *et al*. have tilted sphere-forming BCP samples in the TEM and compared their images to calculated projections in order to verify the 3D morphology. We have taken real-space characterization of sphere-forming BCPs one step further and investigated the 3D morphology of sphere-forming PS-*b*-PMMA with two different thicknesses (L_z) on homogeneous chemically modified substrates using ADF-STEM tomography.

A previous study of the thickness-dependent morphology of sphere-forming PS-*b*-PMMA films has shown through SEM imaging and molecular simulations that a change in film thickness from L_0 (L_0 is the lattice parameter of BCC unit cell in the bulk, in this case 48 nm) to 1.33 L_0 can induce a morphological change from the bulk BCC morphology to a nonbulk HCP morphology.[47] Since in PS-*b*-PMMA the interfacial energies of both blocks are similar, by using nonpreferential top and bottom interfaces, both bulk and nonbulk morphologies could be assembled by tuning the film's thickness. Figure 9 presents 3D structural characterization using ADF-STEM tomography of SIS-treated sphere-forming PS-*b*-PMMA films and corresponding molecular simulations. When the thickness of the film is commensurate to L_0, *i.e.*, L_z = 48 nm, a BCC structure is formed as can be seen in the visualiza-

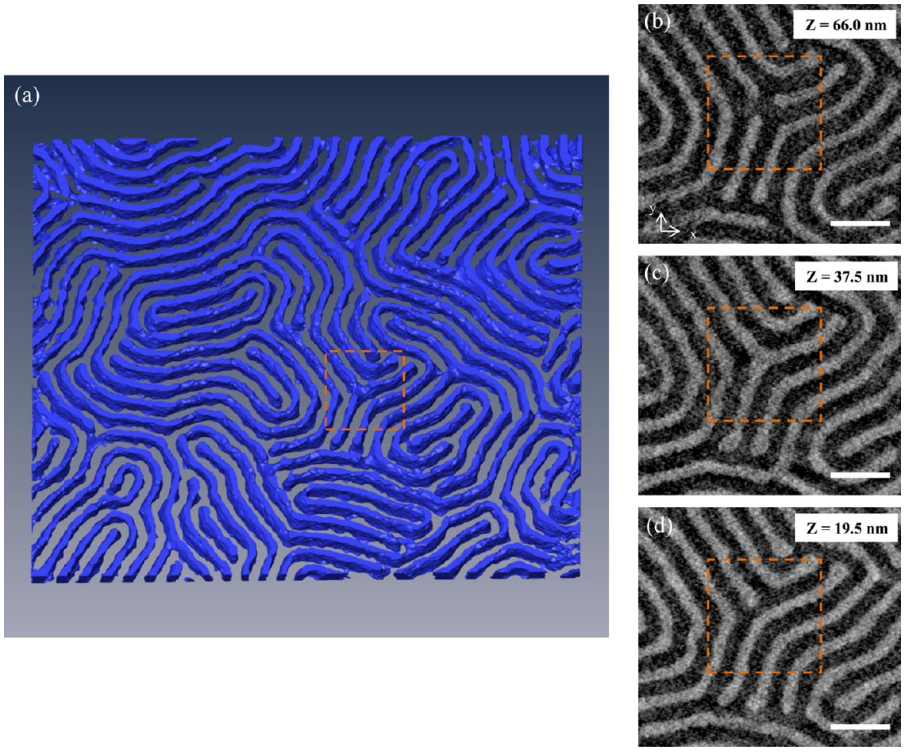

Figure 8. ADF-STEM tomography of lamellae-forming PS-*b*-PMMA treated with three cycles of Al_2O_3 SIS: (a) visualization of the 3D reconstructed volume. For clarity, PMMA domains are colored in blue, while PS domains are transparent. The dimensions of the reconstructed volume is 1506, 1470, and 80 nm (*x*, *y*, *z*). (b, c, d) 1.5 nm thick *xy* slices from the top, middle, and bottom of the film, respectively. The slices show three individual PMMA lamellae close to the film's surface (*z* = 66.0 nm), merging at the middle of the film (*z* = 37.5 nm), and then splitting into two lamellae toward the bottom of the film (*z* = 19.5 nm). Scale bars are 200 nm.

tion of the reconstructed volume (Figure 9a; Movie 5, Supporting Information) and the *xy* and *xz* slices (Figure 9b and c). The 0.78 nm thick *xy* slice, taken at $z = 0.5\ L_z$ (Figure 9b), shows the center spheres in a BCC structure, *i.e.*, the (002) plane, with center-to-center distances (*d*-spacing) of 47.5 ± 2.5 nm and sphere diameters of 23.8 ± 0.9 nm, which is in excellent agreement with theoretical calculations of the sphere diameter.[50] The 0.78 nm thick *xz* slice (Figure 9c) shows a digitally sliced cross section of the (110) plane of the BCC structure, with half-spheres formed at the film's top surface, full spheres formed at $z = 0.5\ L_0$, and half-spheres formed at the substrate interface, *i.e.*, at the interface with the random copolymer mat. It should be noted that since the random copolymer has a PMMA mole fraction of 30%, Al_2O_3 is expected to grow in the random copolymer mat as well. This reduces the contrast between the PMMA half-spheres and the random copolymer mat at the bottom interface and therefore adds to the noise in the reconstruction and visualization of that area. Nonetheless, half-spheres could be identified at the substrate interface.

When the film thickness is tuned to $1.33\ L_0$, an HCP structure is formed as can be seen in the visualization of the reconstructed volume (Figure 9f; Movie 6, Supporting Information) and the digitally sliced *xy* and *xz* slices (Figure 9g and h). The 0.54 nm thick *xy* slice, taken at $z = 0.5\ L_z$ (Figure 9g), shows spheres in the (0002) plane of the HCP structure, with sphere diameters of 23.6 ± 1.0 nm and center-to-center distances (*d*-spacing) of 41.2 ± 2.9 nm. As expected, the spheres' diameter does not change when transitioning from the BCC to the HCP structure, while there is a ~10% reduction in center-to-center distance to accommodate the denser HCP structure. The 0.54 nm thick *xz* slice (Figure 9h) shows a digitally sliced cross section of the $(30\bar{3}0)$ plane of the HCP structure, with full spheres formed at $z = 0.5\ L_z$ and half-spheres formed at the film's top surface. Here, the substrate interface is noisy, but half-spheres could still be identified using band-pass filtering (not shown).

At this point we would like to highlight the impact of the synergy between simulations and the 3D information gained from the technique introduced in this work. In past studies, we have been able to explain phenomena through a concerted simulation and experimental effort, mostly based on comparisons between top-down 2D SEM images and 3D structures obtained by simulations. In a few cases cross-sectional images were also used to investigate the structural ordering inside the polymer film. Simulation models contain approximations and assumptions that have to be validated against experimental results. In particular, we have used a coarse-grained description based on the standard model of block copolymers to describe

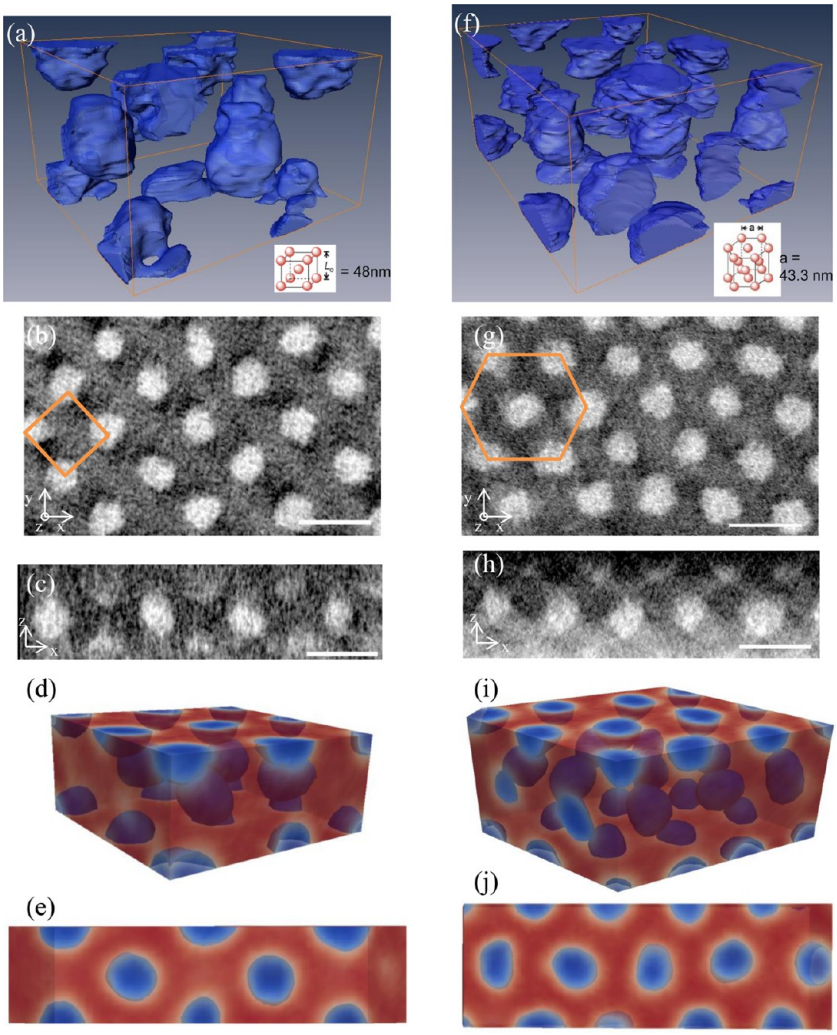

Figure 9. ADF-STEM tomography of sphere-forming PS-*b*-PMMA treated with three cycles of Al_2O_3 SIS and corresponding molecular simulations: (a−e) film thickness equals 1 L_0 (L_0 is the axial length in the cubic unit cell, *i.e.*, 48 nm), where spheres form a BCC morphology; (f−j) film thickness equals 1.5 L_0, where spheres form an HCP morphology. (a, f) Visualization of 2 or 3 unit cells from the reconstructed volume; inset shows an illustration of the morphology. (b, g) 0.78 nm thick and 0.54 nm thick, respectively, *xy* slices taken at *z* equal to half the thickness of the film, showing (002) and (0002), respectively. (c, h) 0.78 nm thick and 0.54 nm thick *xz* slices taken at (110) and (30$\bar{3}$0) planes, respectively. (d, i) 3D and (e, j) slab cross-section (corresponding to those planes at c and h) images obtained by Monte Carlo simulations; nonpreferential top and bottom surfaces were used; red and blue correspond to PS and PMMA domains, respectively.

the self-organization of these materials. This model has been successfully used to predict the behavior in the bulk. In BCP thin films, it is also necessary to describe the properties and effects of the confining surfaces. In our approach, for simplicity, we have assumed that the substrate interface and the polymer−air interface are described by hard walls, and surface chemical affinity is taken into account by an effective one-body interaction characterized by a strength parameter, Λ (see model description in the Experimental Methods for details). By tuning Λ, it is possible to control surface-polymer interfacial energies and therefore the wetting state of the blocks. In the case of symmetric BCPs under nonpreferential conditions, regardless of the Λ value, perpendicularly oriented lamellae are always obtained. However, this is not the case for sphere- and cylinder-forming melts. By increasing Λ, the sphere-forming phase goes from complete wetting to partial wetting and eventually to a dewetting state (Figure S6). From these results, we found that the condition that matches the 3D experimental results is when $\Lambda \approx 1$. Our simulations suggest that Λ controls the line tension of the nanoscale spherical domains on the substrates and is therefore critical for defining the wetting behavior of BCP domains. By using this experimentally informed parameter value, we explored if the model is able to predict the structural transition as film thickness increases. First, we performed simulations for a film thickness $L_z = 1.0\ L_0$, and simulations predict the ordering of spherical domains into a BCC lattice, as can be seen in Figure 9d and e, in agreement with experimental results. By increasing film thickness to $L_z = 1.33\ L_0$ a structural transition is observed numerically, where spherical domains arrange into layers of

hexagonal lattices. Thus, simulations also predict this morphological transition and agree well with experiments, as can be seen in Figure 9i and j.

CONCLUSIONS

In summary, the introduction of Al_2O_3 into the polar domains of PS-*b*-PMMA BCPs *via* the SIS process enabled detailed investigation of BCP films through ADF-STEM tomography. STEM elemental mapping has shown that the Al_2O_3 grows mainly in the PMMA domains of PS-*b*-PMMA BCP films and therefore selectively enhances their contrast, similar to the heavy-metal staining frequently employed in biological electron microscopy. The Al_2O_3 dramatically increases the atomic number (*Z*) contrast of the film without notable change in the BCP's domain size and spacing. Therefore, this approach can be exploited both as an inorganic staining method in BCPs for STEM imaging and for etch-contrast enhancement for BCP pattern transfer.

ADF-STEM tomography performed on SIS-treated lamellae-forming, cylinder-forming, and sphere-forming PS-*b*-PMMA films provided detailed data on the three-dimensional morphology of the phase and grain boundaries and on defects' 3D structure and highlighted the importance of 3D characterization, even for films as thin as 50 nm. Delaunay triangulation and unit-cell orientation analysis of *xy* slice series in the SIS-treated cylinder-forming PS-*b*-PMMA film revealed complex behavior of 5-fold/7-fold coordination defect pairs at grain boundaries as a function of *z*, including parallel cylinders at the top of the film that transform to perpendicular cylinders under the surface of the film, perpendicular cylinders that split into two cylinders toward the bottom of the film, and tilted cylinders that move from grain to grain at the grain boundary. In SIS-treated sphere-forming PS-*b*-PMMA films, the exact phase morphology as a function of the films' thickness was deciphered using ADF-STEM tomography and was correlated with molecular simulations. These results demonstrate the ability of ADF-STEM tomography to provide accurate 3D real-space characterization and provide data for molecular simulation optimization. The experimental and quantitative analysis methodologies presented in this work can be applied to investigate both self-assembled and directed self-assembled BCP structures, enabling nanometric-level understanding and leading to better design, synthesis, and assembly of BCP nanostructures.

EXPERIMENTAL METHODS

Materials. Poly(styrene-*block*-methyl methacrylate) (PS-*b*-PMMA) copolymers were purchased from Polymer Source, Inc., and used as received. The M_n, PDI, and bulk spacing (L_0) of the three PS-*b*-PMMA BCPs used in this work were as follows: lamellae-forming PS-*b*-PMMA: 37k-*b*-37k, 1.08, 40 nm; cylinder-forming PS-*b*-PMMA: 46k-*b*-21k, 1.09, 38 nm; and sphere-forming PS-*b*-PMMA: 71.5k-*b*-12k, 1.17, 48 nm, respectively. Cross-linkable poly(styrene-*ran*-methyl methacrylate) with 4 mol % glycidyl methacrylate cross-linker and different PS *vs* PMMA compositions were synthesized by nitroxide-mediated polymerization.[51,52] They have a mole faction of ~57% (PG4, 57%) or a mole fraction of ~70% (PG4, 70%) styrene by ^{1}H NMR analysis. Poly(acrylic acid) sodium salt solution ($M_w \approx$ 15 000 g/mol, 35% mass fraction in water) was purchased from Sigma-Aldrich and used as received. Toluene was purchased from Fisher Scientific and was used as received.

Sample Preparation. To prepare samples for TEM imaging, silicon wafers were cleaned with piranha solution and rinsed extensively with deionized water. A 5% mass fraction solution of poly(acrylic acid) sodium salt (PAA-Na) in water was spin cast to create a 100 nm thick water-soluble layer and annealed at 160 °C for 5 min. The substrate chemistry was modified by spin-casting a mat layer (PG4, 57%, or PG4, 70%) on the silicon-PAA-Na substrate. The mat polymer was spin-cast from a 0.25% mass fraction solution in toluene to create an 8 to 10 nm thick layer, followed by annealing at 250 °C for 10 to 30 min under a nitrogen atmosphere. Un-cross-linked PS-r-PMMA was removed by sonicating the substrate in toluene. PS-*b*-PMMA films with thicknesses of 80 nm (lamellae), 50 nm (cylinders), and 48 to 64 nm (spheres) were spin-cast from toluene solutions with concentrations of 1% to 2% mass fraction on the silicon-PAA-mat substrates. Samples were annealed at 235 to 250 °C for 10 min under a nitrogen atmosphere (lamellae, cylinders) and at 190 °C for 12 h under vacuum (spheres). The BCP film and mat were floated in deionized water and collected with a silicon nitride supporting film (100 μm silicon frame, 50 nm silicon nitride supporting film in 0.5 mm × 0.55 mm window). Al_2O_3 SIS was performed using alternating exposures to TMA (Aldrich, 97%) and deionized H_2O at 85 °C. The SIS was performed in semistatic mode.[53] N_2 gas (99.999% purity) at 2.25×10^{-4} mol/s (300 sccm) flow was used as purge and carrier gas. To achieve thermal equilibrium, the BCP samples were loaded into the reactor 30 min before commencing the experiment. The base pressure of the reactor was set at ~2.6 Pa (20 mTorr) before introducing precursor vapor. Using a predetermined exposure period, TMA at a pressure of ~665 Pa (5 Torr) was admitted into the reactor, after which the TMA dosing valve was closed, and then pure N_2 gas flowed through the reactor at ~133 Pa (1 Torr) for a predetermined purge period. A similar exposure/purge process was used for the H_2O to complete the SIS cycle. The exposure and purge time used in this experiment was 60 and 300 s, respectively, for both precursors.

Film thickness was measured using an alpha-SE ellipsometer.

Imaging. TEM imaging, STEM imaging, and XEDS-STEM were performed using a field-emission gun TEM operated at 200 kV (FEI Tecnai F20ST- ANL EM Center). XEDS-STEM measurements were performed using a Sapphire 30 mm^2 EDAX detector. Elemental maps were extracted from 128 × 128 pixel (2.3 nm/pixel) XEDS mapping acquired with a 0.8 s dwell time/pixel. Elemental line scans were extracted from a 160 nm XEDS line scan with a 2.0 nm spatial resolution and 10 s dwell time/point.

STEM tomography experiments were performed using a field-emission gun TEM operated at 300 kV (FEI Titan-NIST CNST). In both microscopes the STEM camera length was set to 300 mm. A series of STEM images were acquired at tilt angles ranging from −70° to +70° at angular intervals of 3° from −60° to +60° and at angular intervals of 2° from +60° to +70° and from −60° to −70°. The morphology and feature sizes were unchanged after acquisition compared to the initial state, and therefore the data were not significantly affected by beam damage. The tilt series of the STEM images (51 projections) were aligned using Inspect 3D (FEI) using naturally occurring defects in the block copolymer film and in the silicon nitride supporting film. Reconstruction was performed using a simultaneous iterative reconstruction technique (SIRT) algorithm applied through the same software. The large field of view in

the reconstructed volume showed a small tilting or a curvature in the z (thickness) direction, which is probably due to sample preparation and placement of the sample in the TEM holder. Therefore, the reconstructed stacks' tilting was corrected using interactive stack rotation in ImageJ. Segmentation (thresholding) of the reconstructed volume was performed manually using ImageJ to define the PMMA domains for surface rendering. Visualization of the segmented volume was performed using Amira software.

Quantitative Analysis. The high tilt angles used for tomography in this study (±70°) are predicted to have a relatively small elongation factor of 1.1 due to minimization of the missing wedge, according to a study by Kawase *et al.*[54] However, that study used a filtered back projection reconstruction, and SIRT likely reduces this elongation effect.[55] A recent experimental study by Gotrik *et al.*[21] indicates that the elongation estimated by Kawase *et al.* is probably too large. Thus, the accuracy of dimensional measurements parallel to the optic axis (z-depth) was assumed to be close to the in-plane measurement accuracy; it is worth noting that measurement accuracy is not directly determined by resolution (the ability to distinguish two closely spaced objects), which will be poorer along the optical axis. Due to the large field of view and a slight curvature in the cylindrical sample, the bottom surface of the film, *i.e.*, the interface with the random copolymer mat layer, had also a slight curvature in the xy slice series. The z height difference in the entire field of view was estimated to be 4.4 nm. For convenience, $z = 0$ nm was defined according to the center of the field of view and the xy slice series height was calculated using 1.1 nm z resolution. For quantitative analysis, the xy slice series was segmented using Python script that employed the watershed algorithm. Following segmentation, individual PMMA domains were identified and their center-of-mass was recorded. Center-to-center distances (L_0) were measured by computing the distance between neighboring centers of mass as identified by Delaunay triangulation on the extracted points. Cylinder domain size analysis was performed by measuring the cylinders' circumference and extracting the cylinders' diameter from it under the assumption that the cylinders' face is a circle. Sphere domain size analysis was performed by measuring the area of the sphere section at the spheres' equators and extracting the spheres' diameter under the assumption that the spheres' section is a circle.

We note that the variation in cylinder diameters and spacing primarily reflects the actual variability of the material structure. The absolute measurement accuracy depends on the magnification calibration errors, which we estimate to be approximately 1% to 2% (*e.g.*, <0.8 nm for a 38.5 nm distance). Additional uncertainty comes from errors in the digital analysis method. We estimate the maximum uncertainty in feature spacing measurements to be less than 0.5 pixel and the maximum uncertainty in diameter measurements to be approximately 1 pixel. The magnification calibration error will shift the entire distribution of measurements, and the analysis imprecision will broaden the distribution.

Molecular Simulations. To describe the block copolymer thin films, we use a coarse-grained model where a molecular representation is adopted and the intermolecular interactions are represented by a functional of local densities.[50,51] Macromolecules are represented by flexible linear chains described by the discretized Gaussian chain model composed by N beads, with the position of the tth bead in the ith chain given by $\mathbf{r}_i(t)$. The intermolecular interactions take into account the repulsion between unlike monomers and the finite compressibility of the melt. The system comprises n chains in a volume V at temperature T, and the Hamiltonian defining the model is given by[56,57]

$$\frac{H}{k_BT} = \frac{3}{2}\sum_{i=1}^{n}\sum_{t=1}^{N}\frac{[\mathbf{r}_i(t+1)-\mathbf{r}_i(t)]^2}{b^2} + \rho_0\int_V\left[\chi_{AB}\varphi_A\varphi_B + \frac{\kappa}{2}(1-\varphi_A-\varphi_B)^2\right]d^3\mathbf{r} \quad (2)$$

where b^2 is the mean squared bond length of an ideal chain, ϕ_α is the local density of beads type α (A or B), and ρ_0 is the bead number density. The incompatibility between the polymers is quantified by the Flory−Huggins parameter χ_{AB}, and the melt compressibility by κ. Macromolecules are confined between two hard surfaces, located in the planes $z = 0$ and $z = L_z$, which are impenetrable to the chains; in the other two directions we apply periodic boundary conditions. The influence of the surfaces is represented with a short-range interaction potential, U_S, acting on each bead:[58]

$$\frac{U_S(\mathbf{r},\alpha)}{k_BT} = -\frac{\Lambda_s^\alpha}{d_s/R_e}\exp\left[-\frac{z^2}{2{d_s}^2}\right] \quad (3)$$

The potential decays over a distance d_s, and $\Lambda_s^\alpha N$ determines the strength of the interaction between beads of type α and the surfaces. Under homogeneous conditions, U_S depends only on z, the distance from the surface. The interaction between the blocks (A or B) with the surfaces is specified by four parameters: Λ^A_{top}, Λ^A_{bottom}, Λ^B_{top}, and Λ^B_{bottom}. The interaction range was fixed at $d_s = 0.15R_e$. Equilibrium morphologies were determined by Monte Carlo simulations, and local densities were computed from the beads' positions through a particle-to-mesh interpolation approach.[56] We sampled configurations according to the Metropolis criteria, $P_{acc} = \min[1, \exp(-\Delta H/k_BT)]$, where ΔH is the energy change between two configurations and includes both bonded and nonbonded contributions as well as contributions from the surfaces. We considered these trial moves: local displacements of the beads, reptation-like moves, and translation of an entire chain. To represent the sphere-forming block copolymer, we have used $\kappa N = 40$, $\chi_{AB}N = 32$, and $\rho_0 {R_e}^3/N = 110$ for representing a PS-*b*-PMMA diblock copolymer with a molecular weight equal to 84 kg/mol. The chain is composed by $N = 27 + 5$ beads, and the end-to-end distance R_e set the length scale in the model. For these parameters, the natural period of the BCC morphology in the bulk is $L_0 \approx 1.9R_e$. The simulation box had dimensions $L_x = L_y = 4\,L_0$ (we have also used $L_x = L_y = 8\,L_0$ for exploring finite-size effects, but these were not observed) and L_z. We considered both surfaces to be equivalent and nonpreferential, *i.e.*, $\Lambda^A_{top} = \Lambda^A_{bottom} = \Lambda^B_{top} = \Lambda^B_{bottom} = \Lambda$. We performed a sweep in parameter space of Λ, to establish the effect of substrate surface energy on the wetting of the minority phase (see Figure S6). From these data, we deduce that the condition that matches the 3D experimental results is when $\Lambda \approx 1$; our simulations suggest that Λ controls the line tension of the nanoscale spherical domains on the substrates, therefore being critical for defining wetting behavior of BCP domains.

Disclosure: Certain commercial equipment, instruments, or materials are identified in this report in order to specify the experimental procedure adequately. Such identification is not intended to imply recommendation or endorsement by the National Institute of Standards and Technology, nor is it intended to imply that the materials or equipment identified are necessarily the best available for the purpose.

Conflict of Interest: The authors declare no competing financial interest.

Acknowledgment. T.S.-P. is an Awardee of the Weizmann Institute of Science−National Postdoctoral Award Program for Advancing Women in Science. This work was supported in part by the U.S. Department of Energy, Office of Science, Office of Basic Energy Sciences, at the Materials Science Division, at the Center for Nanoscale Materials, and at the Electron Microscopy Center in the NanoScience and Technology Division, all in Argonne National Laboratory under Contract No. DE-AC02-06CH11357. The project was in part funded by award 70NHNB14H012 from the U.S. Department of Commerce, National Institute of Standards and Technology, as part of the CHiMad. We gratefully acknowledge the computing resources provided on Blues, high-performance computing cluster operated by the Laboratory Computing Resource Center at Argonne National Laboratory.

Supporting Information Available: TEM images prior and after the SIS process, XEDX-STEM elemental analysis, stability measurements, quantitative analysis of tomography data as a function of depth, digitally sliced cross section, numerical

simulations of spherical phase assembly, and six movies of the visualization of reconstructed tomography data and analysis of defects and grain boundaries. The Supporting Information is available free of charge on the ACS Publications website at DOI: 10.1021/acsnano.5b01013.

REFERENCES AND NOTES

1. Herr, D. J. C. Directed Block Copolymer Self-Assembly for Nanoelectronics Fabrication. *J. Mater. Res.* **2011**, *26*, 122–139.
2. Stoykovich, M. P.; Nealey, P. F. Block Copolymers and Conventional Lithography. *Mater. Today* **2006**, *9*, 20–29.
3. Darling, S. B. Directing the Self-Assembly of Block Copolymers. *Prog. Polym. Sci.* **2007**, *32*, 1152–1204.
4. Liu, C.-C.; Ramírez-Hernández, A.; Han, E.; Craig, G. S. W.; Tada, Y.; Yoshida, H.; Kang, H.; Ji, S.; Gopalan, P.; de Pablo, J. J.; Nealey, P. F. Chemical Patterns for Directed Self-Assembly of Lamellae-Forming Block Copolymers with Density Multiplication of Features. *Macromolecules* **2013**, *46*, 1415–1424.
5. Liu, G.; Kang, H.; Craig, G. S. W.; Detcheverry, F.; de Pablo, J. J.; Nealey, P. F.; Tada, Y.; Yoshida, H. Cross-Sectional Imaging of Block Copolymer Thin Films on Chemically Patterned Surfaces. *J. Photopolym. Sci. Technol.* **2010**, *23*, 149–154.
6. Ji, S.; Liu, C.-C.; Liao, W.; Fenske, A. L.; Craig, G. S. W.; Nealey, P. F. Domain Orientation and Grain Coarsening in Cylinder-Forming Poly(Styrene-*b*-Methyl Methacrylate) Films. *Macromolecules* **2011**, *44*, 4291–4300.
7. Han, E.; Stuen, K. O.; Leolukman, M.; Liu, C.-C.; Nealey, P. F.; Gopalan, P. Perpendicular Orientation of Domains in Cylinder-Forming Block Copolymer Thick Films by Controlled Interfacial Interactions. *Macromolecules* **2009**, *42*, 4896–4901.
8. Harrison, C.; Park, M.; Chaikin, P.; Register, R. A.; Adamson, D. H.; Yao, N. Depth Profiling Block Copolymer Microdomains. *Macromolecules* **1998**, *31*, 2185–2189.
9. Magerle, R. Nanotomography. *Phys. Rev. Lett.* **2000**, *85*, 2749–2752.
10. Liedel, C.; Hund, M.; Olszowka, V.; Boker, A. On the Alignment of a Cylindrical Block Copolymer: A Time-Resolved and 3-Dimensional Sfm Study. *Soft Matter* **2012**, *8*, 995–1002.
11. Sunday, D. F.; Hammond, M. R.; Wang, C.; Wu, W.-l.; Delongchamp, D. M.; Tjio, M.; Cheng, J. Y.; Pitera, J. W.; Kline, R. J. Determination of the Internal Morphology of Nanostructures Patterned by Directed Self Assembly. *ACS Nano* **2014**, *8*, 8426–8437.
12. Frank, E. J. *Electron Tomography, Three Dimensional Imaging with the Transmission Electron Microscope*; Plenum Press, 1992.
13. Lo, T.-Y.; Ho, R.-M.; Georgopanos, P.; Avgeropoulos, A.; Hashimoto, T. Direct Visualization of Order−Order Transitions in Silicon-Containing Block Copolymers by Electron Tomography. *ACS Macro Lett.* **2013**, *2*, 190–194.
14. Park, H.-W.; Jung, J.; Chang, T.; Matsunaga, K.; Jinnai, H. New Epitaxial Phase Transition between Dg and Hex in Ps-B-Pi. *J. Am. Chem. Soc.* **2008**, *131*, 46–47.
15. Higuchi, T.; Motoyoshi, K.; Sugimori, H.; Jinnai, H.; Yabu, H.; Shimomura, M. Phase Transition and Phase Transformation in Block Copolymer Nanoparticles. *Macromol. Rapid Commun.* **2010**, *31*, 1773–1778.
16. Mareau, V. H.; Akasaka, S.; Osaka, T.; Hasegawa, H. Direct Visualization of the Perforated Layer/Gyroid Grain Boundary in a Polystyrene-Block-Polyisoprene/Polystyrene Blend by Electron Tomography. *Macromolecules* **2007**, *40*, 9032–9039.
17. Li, L.; Matsunaga, K.; Zhu, J.; Higuchi, T.; Yabu, H.; Shimomura, M.; Jinnai, H.; Hayward, R. C.; Russell, T. P. Solvent-Driven Evolution of Block Copolymer Morphology under 3D Confinement. *Macromolecules* **2010**, *43*, 7807–7812.
18. Higuchi, T.; Motoyoshi, K.; Sugimori, H.; Jinnai, H.; Yabu, H.; Shimomura, M. Three-Dimensional Observation of Confined Phase-Separated Structures in Block Copolymer Nanoparticles. *Soft Matter* **2012**, *8*, 3791–3797.
19. Drummy, L. F.; Wang, Y. C.; Schoenmakers, R.; May, K.; Jackson, M.; Koerner, H.; Farmer, B. L.; Mauryama, B.; Vaia, R. A. Morphology of Layered Silicate− (Nanoclay−) Polymer Nanocomposites by Electron Tomography and Small-Angle X-Ray Scattering. *Macromolecules* **2008**, *41*, 2135–2143.
20. Niihara, K.-i.; Matsuwaki, U.; Torikai, N.; Atarashi, H.; Tanaka, K.; Jinnai, H. A Novel Structural Analysis for a Cylinder-Forming Block Copolymer Thin Film Using Neutron Reflectivity Aided by Transmission Electron Microtomography. *Macromolecules* **2007**, *40*, 6940–6946.
21. Gotrik, K. W.; Lam, T.; Hannon, A. F.; Bai, W.; Ding, Y.; Winterstein, J.; Alexander-Katz, A.; Liddle, J. A.; Ross, C. A. 3D Tem Tomography of Templated Bilayer Films of Block Copolymers. *Adv. Funct. Mater.* **2014**, *24*, 7689–7697.
22. Staniewicz, L.; Donald, A. M.; Stokes, D. J. The Effect of Osmium Staining on Lamellar Spacing in Thin Polystyrene-Polyisoprene Diblock Copolymer Films. *J. Phys. Conf. Ser.* **2010**, *241*, 012077-1–4.
23. George, S. M. Atomic Layer Deposition: An Overview. *Chem. Rev.* **2009**, *110*, 111–131.
24. Peng, Q.; Tseng, Y.-C.; Darling, S. B.; Elam, J. W. Nanoscopic Patterned Materials with Tunable Dimensions via Atomic Layer Deposition on Block Copolymers. *Adv. Mater.* **2010**, *22*, 5129–5133.
25. Peng, Q.; Tseng, Y.-C.; Darling, S. B.; Elam, J. W. A Route to Nanoscopic Materials via Sequential Infiltration Synthesis on Block Copolymer Templates. *ACS Nano* **2011**, *5*, 4600–4606.
26. Tseng, Y.-C.; Peng, Q.; Ocola, L. E.; Czaplewski, D. A.; Elam, J. W.; Darling, S. B. Enhanced Polymeric Lithography Resists via Sequential Infiltration Synthesis. *J. Mater. Chem.* **2011**, *21*, 11722–11725.
27. Tseng, Y.-C.; Peng, Q.; Ocola, L. E.; Elam, J. W.; Darling, S. B. Enhanced Block Copolymer Lithography Using Sequential Infiltration Synthesis. *J. Phys. Chem. C* **2011**, *115*, 17725–17729.
28. Ruiz, R.; Wan, L.; Lille, J.; Patel, K. C.; Dobisz, E.; Johnston, D. E.; Kisslinger, K.; Black, C. T. Image Quality and Pattern Transfer in Directed Self Assembly with Block-Selective Atomic Layer Deposition. *J. Vac. Sci. Technol. B* **2012**, *30*, -.
29. Tseng, Y.-C.; Mane, A. U.; Elam, J. W.; Darling, S. B. Enhanced Lithographic Imaging Layer Meets Semiconductor Manufacturing Specification a Decade Early. *Adv. Mater.* **2012**, *24*, 2608–2613.
30. Al_2O_3 grown in ALD in low temperatures (85−150 °C) is known to have increased hydrogen content with decreasing temperature (*Chem. Mater.* **2004**, *16*, 639−645). Nonetheless, in this work, for the sake of simplicity, we refer to alumina grown in 85° C as Al_2O_3.
31. Biswas, M.; Libera, J. A.; Darling, S. B.; Elam, J. W. Kinetics for the Sequential Infiltration Synthesis of Alumina in Poly(Methyl Methacrylate)−an Infrared Spectroscopic Study. *J. Phys. Chem. C* **2015**in press.
32. Jinnai, H.; Jiang, X. Electron Tomography in Soft Materials. *Curr. Opin. Solid State Mater. Sci.* **2013**, *17*, 135–142.
33. Jinnai, H.; Spontak, R. J. Transmission Electron Microtomography in Polymer Research. *Polymer* **2009**, *50*, 1067–1087.
34. Reimer, L.; Kohl, H. *Transmission Electron Microscopy: Physics of Image Formation*, 5th ed.; Springer: New York, 2008.
35. Motoki, S.; Kaneko, T.; Aoyama, Y.; Nishioka, H.; Okura, Y.; Kondo, Y.; Jinnai, H. Dependence of Beam Broadening on Detection Angle in Scanning Transmission Electron Microtomography. *J. Electron Microsc.* **2010**, *59*, S45–53.
36. Loos, J.; Sourty, E.; Lu, K.; Freitag, B.; Tang, D.; Wall, D. Electron Tomography on Micrometer-Thick Specimens with Nanometer Resolution. *Nano Lett.* **2009**, *9*, 1704–1708.
37. Aoyama, K.; Takagi, T.; Hirase, A.; Miyazawa, A. Stem Tomography for Thick Biological Specimens. *Ultramicroscopy* **2008**, *109*, 70–80.

38. Yakushevska, A. E.; Lebbink, M. N.; Geerts, W. J. C.; Spek, L.; van Donselaar, E. G.; Jansen, K. A.; Humbel, B. M.; Post, J. A.; Verkleij, A. J.; Koster, A. J. Stem Tomography in Cell Biology. *J. Struct. Biol.* **2007**, *159*, 381–391.
39. Thurn-Albrecht, T.; Steiner, R.; DeRouchey, J.; Stafford, C. M.; Huang, E.; Bal, M.; Tuominen, M.; Hawker, C. J.; Russell, T. P. Nanoscopic Templates from Oriented Block Copolymer Films. *Adv. Mater.* **2000**, *12*, 787–791.
40. Grubb, D. T. Radiation Damage and Electron Microscopy of Organic Polymers. *J. Mater. Sci.* **1974**, *9*, 1715–1736.
41. Pells, G. P.; Stathopoulos, A. Y. Radiation Damage in the Cation Sublattice of Alpha-Al_2O_3. *Radiat. Eff.* **1983**, *74*, 181–191.
42. Hammond, M. R.; Sides, S. W.; Fredrickson, G. H.; Kramer, E. J.; Ruokolainen, J.; Hahn, S. F. Adjustment of Block Copolymer Nanodomain Sizes at Lattice Defect Sites. *Macromolecules* **2003**, *36*, 8712–8716.
43. Aissou, K.; Baron, T.; Kogelschatz, M.; Pascale, A. Phase Behavior in Thin Films of Cylinder-Forming Diblock Copolymer: Deformation and Division of Heptacoordinated Microdomains. *Macromolecules* **2007**, *40*, 5054–5059.
44. Karim, A.; Martin, K.; Thierry, B. Self-Assembling Study of a Cylinder-Forming Block Copolymer via a Nucleation–Growth Mechanism. *Nanotechnology* **2009**, *20*, 095602-1–9.
45. Bosworth, J. K.; Dobisz, E. A.; Hellwig, O.; Ruiz, R. Impact of Out-of-Plane Translational Order in Block Copolymer Lithography. *Macromolecules* **2011**, *44*, 9196–9204.
46. Nelson, D. R.; Halperin, B. I. Dislocation-Mediated Melting in Two Dimensions. *Phys. Rev. B* **1979**, *19*, 2457–2484.
47. Ji, S.; Nagpal, U.; Liao, W.; Liu, C.-C.; de Pablo, J. J.; Nealey, P. F. Three-Dimensional Directed Assembly of Block Copolymers Together with Two-Dimensional Square and Rectangular Nanolithography. *Adv. Mater.* **2011**, *23*, 3692–3697.
48. Stein, G. E.; Kramer, E. J.; Li, X.; Wang, J. Layering Transitions in Thin Films of Spherical-Domain Block Copolymers. *Macromolecules* **2007**, *40*, 2453–2460.
49. Stein, G. E.; Lee, W. B.; Fredrickson, G. H.; Kramer, E. J.; Li, X.; Wang, J. Thickness Dependent Ordering in Laterally Confined Monolayers of Spherical-Domain Block Copolymers. *Macromolecules* **2007**, *40*, 5791–5800.
50. Bates, F. S.; Cohen, R. E.; Berney, C. V. Small-Angle Neutron Scattering Determination of Macrolattice Structure in a Polystyrene-Polybutadiene Diblock Copolymer. *Macromolecules* **1982**, *15*, 589–592.
51. Ji, S.; Liao, W.; Nealey, P. F. Block Cooligomers: A Generalized Approach to Controlling the Wetting Behavior of Block Copolymer Thin Films. *Macromolecules* **2010**, *43*, 6919–6922.
52. Ji, S.; Liu, C.-C.; Son, J. G.; Gotrik, K.; Craig, G. S. W.; Gopalan, P.; Himpsel, F. J.; Char, K.; Nealey, P. F. Generalization of the Use of Random Copolymers to Control the Wetting Behavior of Block Copolymer Films. *Macromolecules* **2008**, *41*, 9098–9103.
53. Kemell, M.; Ritala, M.; Leskelä, M.; Groenen, R.; Lindfors, S. Coating of Highly Porous Fiber Matrices by Atomic Layer Deposition. *Chem. Vap. Deposition* **2008**, *14*, 347–352.
54. Kawase, N.; Kato, M.; Nishioka, H.; Jinnai, H. Transmission Electron Microtomography without the "Missing Wedge" for Quantitative Structural Analysis. *Ultramicroscopy* **2007**, *107*, 8–15.
55. Midgley, P. A.; Weyland, M. 3d Electron Microscopy in the Physical Sciences: The Development of Z-Contrast and Eftem Tomography. *Ultramicroscopy* **2003**, *96*, 413–431.
56. Detcheverry, F. A.; Kang, H.; Daoulas, K. C.; Müller, M.; Nealey, P. F.; de Pablo, J. J. Monte Carlo Simulations of a Coarse Grain Model for Block Copolymers and Nanocomposites. *Macromolecules* **2008**, *41*, 4989–5001.
57. Fredrickson, G. H. *The Equilibrium Theory of Inhomogeneous Polymers*; Clarendon Press, 2006.
58. Daoulas, K. C.; Muller, M.; de Pablo, J. J.; Nealey, P. F.; Smith, G. D. Morphology of Multi-Component Polymer Systems: Single Chain in Mean Field Simulation Studies. *Soft Matter* **2006**, *2*, 573–583.